





Stability of gravity-driven viscous films flowing down a soft cylinder

Yochuang Chao ^{1,*}, Lailai Zhu ², Zijing Ding ¹, Tiantian Kong,³
Juntao Chang,^{1,†} and Ziao Wang ¹

¹*School of Energy Science and Engineering, Harbin Institute of Technology, Harbin 150001, China*

²*Department of Mechanical Engineering, National University of Singapore, 117575, Singapore*

³*Department of Biomedical Engineering, School of Medicine, Shenzhen University, Shenzhen 518060, China*



(Received 28 April 2024; accepted 22 August 2024; published 9 September 2024)

We study the stability of gravity-driven viscous liquid films flowing down a vertical cylinder that is uniformly coated with a thin layer of elastic solids. Combining the gravity-driven viscous flows with the elastic deformation of the coated soft layer, we formulate a long-wave model to describe the evolution of a film flow-soft structure coupled system. Based on the model, we systematically examine the impact of the coating properties, including the elasticity and thickness on the temporal and spatiotemporal stability. Temporal stability analysis shows that the soft layer plays a dual role, namely, the elasticity acts as a destabilizing factor, leading to large deformations of both film interface and soft surface. However, due to the geometrical effect, increasing the layer thickness stabilizes the Rayleigh-Plateau instability. By contrast, the linear phase speed is always enhanced with increasing the elasticity or the thickness of the coated layer. We then analyze the spatiotemporal nature of free-surface instabilities and find that the elasticity can trigger the film flows from being absolutely unstable to convectively unstable. Transient numerical solutions of the full asymptotic model further verify the predictions from linear stability analysis, and more importantly, reveal the nonlinear effect of the softness. Compared to liquid films falling down the cylinder with rigid walls, the soft surface can enhance the coalescence of faster, larger sliding droplets with preceding slower, smaller sliding ones, thus resulting in a more unstable system. Our study highlights the potential of coating a thin layer of soft materials onto the walls of substrate to regulate the dynamics of liquid film systems, and may have implications for the emerging bioinspired applications; for instance, the large-scale collection and transport of water on flexible microfiber arrays.

DOI: [10.1103/PhysRevFluids.9.094001](https://doi.org/10.1103/PhysRevFluids.9.094001)

I. INTRODUCTION

Viscous liquid films falling along the exterior wall of a vertical cylinder are widely present in nature, and impact various engineering processes, such as the fiber coating [1], heat exchanger [2], and water treatment [3]. Liquid films initially coated on the cylindrical surface will inevitably undergo the surface-tension-induced Rayleigh-Plateau instability [4,5], which drives film flows into an array of large droplets. In particular, the free surface of such flows is unstable to the disturbances with long wavelengths, which often grow initially and eventually saturate well outside the linear regime. To further consider the nonlinear evolution of the free surface, several asymptotic models that can largely reduce the complexity of Navier-Stokes equations have been developed [6], such as the thin-film model [7] assuming the film thickness is much smaller than the cylinder radius, which

*Contact author: ychoa@hit.edu.cn

†Contact author: changjuntao@hit.edu.cn

can capture the primary features of thin-film flows; the long-wave model [8] that contains more complicated nonlinear terms and has been widely applied for both thin and thick film flows at low Reynolds numbers; as well as the integral-boundary model [9] and the recently proposed weighted-residual integral-boundary-layer model [10], which are combined with the assumption of a self-similar velocity profile and can model liquid films at moderate and even high Reynolds numbers. These asymptotic models have been demonstrated to effectively capture a variety of dynamical phenomena observed experimentally for the scenario of liquid films falling down a vertical cylinder; for instance, the formation of coherent structures including the dropletlike pulses and bound states [11], as well as the coalescence of droplets and emergence of irregular wavy patterns triggered by temperature gradients [12].

Due to the wide presence of liquid films on the surface of cylindrical geometries as well as its exhibition of rich interfacial dynamics in industrial applications, a variety of theoretical and experimental studies in the scope of the above-mentioned long-wave models have been performed in recent years [6]. For instance, Goren [13] explored thin films down the outer surface of a cylinder, which is probably one of the first to show that a perturbation with certain wavelengths aroused from Rayleigh-Plateau instability grows faster than other perturbations. Trifonov [14] later on examined the wave characteristics of liquid film falling down vertical wires and tubes, and found that the intensity of surface waves can be enhanced with decreasing cylinder radius. Frenkel [7] proposed a thin-film model to study the free surface of a thin axisymmetric film falling down a vertical tube and showed that the model is applicable to the strong undulating films. Then, Kalliadasis and Chang [15] explored the self-similar solutions of the thin-film model and demonstrated that static capillary forces may drain the film fluids into droplets. Early experiments conducted by Kliakhandler *et al.* [16] reported that there are three qualitatively different regimes of sliding droplet patterns for the situation of thick films. This study was revisited by Craster and Matar [8], in which a long-wavelength model was formulated and this model successfully captured the main flow regimes as well as the transition between different patterns observed in experiments. Spatiotemporal stability analysis of falling films using the asymptotic model in combination with the experiments were first performed by Duprat *et al.* [11]. Similar with other open-flow hydrodynamic systems, they revealed that the instabilities of viscous liquid films down a vertical fiber can also be classified as convective or absolute, which depend on the film thickness and fiber radius. At large or small film thickness, the convective instability can be observed. However, in an intermediate film thickness but for small enough fiber radius, the instability is absolute. In addition, Sisoev *et al.* [9] investigated the axisymmetric flow of fluid films and demonstrated the selection mechanism leading to the development of so-called “dominating” traveling waves in experiments. Ruyer-Quil *et al.* [10] further proposed a two-equation model, namely, a weighted-residual integral-boundary-layer model that accounts for both inertial and streamwise viscous effects, showing good agreement between numerical simulations and experiments. More recently, Kim *et al.* [17] and Biswal *et al.* [18] developed positivity-preserving numerical schemes and optimal boundary control strategies, which show that traveling wave profiles can be controlled to within a small domain. These early studies have combined to successfully shed light on the primary mechanisms of instability growth and saturation for liquid films coating down a cylindrical surface in a variety of contexts.

With the above general picture, further studies are devoted to resolving the remaining discrepancies between theoretical predictions and experimental observations, where additional effects such as the wall slip [19] and disjoining pressure [20] were examined. As an example, taking wall slip into account, Halpern and Wei [19] provided a plausible interpretation as to why the critical Bond number for droplet formation predicted by previous no-slip models [15,21] is slightly smaller than that observed from experiments [22]. In addition, part of the studies are also investigating other effects on the interfacial dynamics of falling liquid films, including the thermocapillarity [23], chemical reactions [24], non-Newtonian fluids [25], as well as the rotational or geometric effect [26,27]. For instance, Gabbard and Bostwick [25] explored a highly shear-thinning non-Newtonian liquid

film and found that the rheological properties of fluids can significantly impact the morphology of sliding beads on fibers. Eghbali *et al.* [27] experimentally explored viscous films down an eccentric fiber, revealing two asymmetric unstable modes in such configuration—namely, the pearl and whirl modes. The thermocapillary effect on the spatiotemporal stability was recently examined by Liu *et al.* [28] and Ding *et al.* [29], showing that with the increase of wall heating, the falling film tends to break up into droplets because of the enhanced absolute instability. Recent experiments by Ji *et al.* [12] further demonstrated that imposing a thermal gradient along the fiber can trigger the formation of irregular wavy patterns and coalescence of sliding beads in the absolute regime.

However, much less is understood about how a liquid film flows down a compliant cylindrical surface where the coupling of substrate deformation and free-surface flows might be crucial. The effect of wall compliance has been extensively studied for thin-film flows inside flexible tubes [30,31] and on compliant inclined substrates [32–36], revealing that wall flexibility significantly impacts the interfacial dynamics of liquid films. For instance, using the lubrication theory, Halpern and Grotberg [30] explored the instability of film flows in compliant pulmonary airways, showing that wall flexibility may cause the airway to collapse, and the closure occurs more rapidly with increasing the wall flexibility. Deriving Benney-like coupled equations, Matar *et al.* [32] showed that wall flexibility can enhance the instability of falling fluid films over an inclined, flexible substrate, suggesting that wall compliance might be an alternative route to enhance the interfacial heat and/or mass transport. A very recent work by Bharti *et al.* [37] investigated the role of surface softness on the instability of thin films coated on a horizontal soft fiber. In their study, linear stability analysis indicates that surface softness can destabilize the system and increasing the thickness of the soft layer reduces the linear growth rate. Notably, in the last few years, an increasing number of studies have revealed a variety of intriguing interfacial phenomena on fluid-soft structure interactions [38,39]. One of the typical scenarios is the wetting dynamics on the surface of soft solids, i.e., elastocapillarity, such as the stick-slip motion of three-phase contact lines on ultrasoft gels [40], and collective droplet durotaxis on stiffness gradient substrates [41]. For another typical scenario, namely, soft lubrication that is free of contact lines, also illustrates a series of unexpected effects, for instance, self-sustained lift motion of a fluid-immersed cylinder on a soft incline [42]. These emerging findings demonstrate the great promise in investigating the coupling of elastic, viscous, and surface tension forces for a wide range of applications, such as microfluidics, 3D printing, and water harvesting [38,39].

Despite the growing interest in fluid-elastic interactions at compliant interfaces, a full understanding of the interfacial dynamics of a falling liquid film on a soft cylindrical solid, particularly for the canonical fiber-coating problem, is still missing. In particular, thin-film flows are inevitably accompanied by the deformation of soft interfaces, which naturally raises the question of how this deformation correlates with the dynamics of such surface flows, for instance, the linear and nonlinear interfacial instabilities. Therefore, in this paper, we are motivated to examine the role of surface elasticity in the instabilities of gravity-driven viscous films down the surface of a vertical, soft-layer-coated cylinder. Note that most of the previous studies, for instance, those by Halpern and Grotberg [30] and Matar *et al.* [32], assumed that the whole substrate is thin and flexible, and a forced membrane equation for the wall deformation is applied. By contrast, we here focus on the local deformation of the soft wall, for instance, by Skotheim and Mahadevan [43] and Bharti *et al.* [37], and the configuration of a thin, soft layer coated on the surface of a vertical rigid cylinder is examined, as shown in Fig. 1. In Sec. II, we begin with the mathematical formulation and develop a long-wave asymptotic model that incorporates the elastic deformation of a soft interface. To characterize the impact of the thickness and elasticity of the coated soft layer on the flow characteristics, we further perform both temporal and spatiotemporal stability analyses of the linearized model equation in Sec. III. These linear stability analyses are further complemented by numerically solving the full nonlinear model equation, with detailed discussion on the impact of the coated soft layer on the formation of sliding droplets in Sec. IV. We give our conclusions in Sec. V.

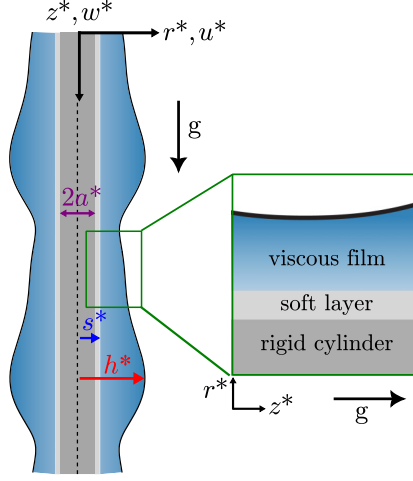


FIG. 1. Schematic of the geometry: a gravity-driven film (light blue) of initial thickness h_0^* flowing along a vertical cylinder (gray) of radius a^* . The cylindrical surface is uniformly coated with a soft layer (light gray) of initial thickness s_0^* . The flow is surrounded by a passive gas, and the distances from the cylinder center to the fluid-air free surface and to the fluid-soft layer interface are denoted by $h^*(z^*, t^*)$ and $s^*(z^*, t^*)$, respectively.

II. PROBLEM FORMULATION

We consider a two-dimensional axisymmetric Newtonian viscous liquid film flowing along the surface of a rigid cylinder, which is coated with a thin layer of soft and compressible solid. This soft solid layer is assumed to be isotropic and linearly elastic, with shear and bulk moduli G and λ , respectively. The liquid properties, including the density ρ , surface tension σ , and dynamic viscosity μ are assumed to be constant. In addition, we assume that the surrounding air is passive and inviscid, and thus its effect is neglected. The radius of rigid cylindrical core, initial thickness of coated layer, and initial thickness of liquid film are denoted by a^* , s_0^* , and h_0^* , respectively. Then, the initial radius of the fluid ring measured from the center of the cylinder is $h_0^* = a^* + s_0^* + h_0^*$. The axisymmetric system is described in a cylindrical coordinate (r^*, z^*) , where the r^* direction is perpendicular to and the z^* direction is parallel to the cylindrical wall, i.e., the direction of gravity, respectively. As shown in Fig. 1, $r^* = h^*(z^*, t^*)$ and $r^* = s^*(z^*, t^*)$ denote the distances from the center to the liquid film–air free surface and liquid film–soft-layer interface, respectively.

A. Governing equations

The dimensional continuity and Navier-Stokes equations for the axisymmetric flow are

$$u_r^* + \frac{u^*}{r^*} + w_{z^*}^* = 0, \quad (1a)$$

$$u_t^* + u^* u_{r^*}^* + w^* u_{z^*}^* = -\frac{1}{\rho} p_{r^*}^* + \frac{\mu}{\rho} \left(u_{r^* r^*}^* + \frac{u_{r^*}^*}{r^*} - \frac{u^*}{r^{*2}} + u_{z^* z^*}^* \right), \quad (1b)$$

$$w_t^* + u^* w_{r^*}^* + w^* w_{z^*}^* = -\frac{1}{\rho} p_{z^*}^* + \frac{\mu}{\rho} \left(w_{r^* r^*}^* + \frac{w_{r^*}^*}{r^*} + w_{z^* z^*}^* \right) + g, \quad (1c)$$

where u^* and w^* represent the radial and axial components of the velocity, respectively; t^* is the time; and p^* and g are the pressure and gravitational acceleration, respectively. Quantities with dimensions are denoted with an asterisk and subscripts denote partial derivatives.

Along the cylinder, at the interface between the soft layer and liquid film $r^* = s^*(z^*, t^*)$, we apply the no-slip and no-penetration boundary conditions

$$u^* = w^* = 0. \quad (2)$$

At the liquid film–air free surface $r^* = h^*(z^*, t^*)$, the continuity of tangential stresses is required:

$$2h_{z^*}^*(u_{r^*}^* - w_{z^*}^*) + (1 - h_{z^*}^{*2})(u_{z^*}^* + w_{r^*}^*) = 0, \quad (3)$$

and a jump in normal stress according to the Young-Laplace law is formulated as

$$p^* + \frac{2\mu}{1 + h_{z^*}^{*2}} [h_{z^*}^*(u_{z^*}^* + w_{r^*}^*) - u_{r^*}^* - h_{z^*}^{*2}w_{z^*}^*] = \sigma \left[\frac{1}{h^*(1 + h_{z^*}^{*2})^{1/2}} - \frac{h_{z^*}^*}{(1 + h_{z^*}^{*2})^{3/2}} \right], \quad (4)$$

where both the destabilizing azimuthal curvature term and the stabilizing axial curvature term are included in the right part.

At the liquid film–air free surface $r^* = h^*(z^*, t^*)$, the kinematic boundary condition is given by

$$h_{t^*}^* + w^*h_{z^*}^* = u^*. \quad (5)$$

To complete the description of the problem, at the liquid film–soft layer interface $r^* = s^*(z^*, t^*)$, we need to specify the relation between the fluid stresses and the deformation of the coated soft layer. Here, we follow the classical studies in soft lubrication (see, for instance, Skotheim and Mahadevan [43] and Bharti *et al.* [37]), assuming that the soft layer is thin and compressible and thus its displacement $\delta^*(z^*, t^*)$ can be related to a localized, linear elastic response to the fluid pressure p^* , expressed as

$$\delta^* \propto -\frac{p^*}{2G + \lambda}, \quad (6)$$

where the convention that δ^* is negative is used, and the bulk modulus λ of the elastic layer can be calculated by $\lambda = 2G\nu/(1 - 2\nu)$ with ν the Poisson ratio. The linear relationship between the normal displacement δ^* and fluid pressure p^* , namely, Eq. (6), is known as the Winkler or “mattress” elastic foundation model [44]. The key hypothesis in this model is that the elastic layer is thin compared to the characteristic length scale [45], as later will be shown in the case of our problem, namely, $s_0^* \ll \ell_c^*$, where ℓ_c^* is the characteristic (capillary) length. Although Eq. (6) is mathematically simplified, it has been widely adopted for the small deformation of thin-enough compressible elastic film [37,46,47]. In addition, it has also successfully described experiments where the thin coated layer is elastomeric and so might, ordinarily, be considered to be close to incompressible; for instance, polydimethylsiloxane (PDMS) and polyacrylamide (PAA) polymer gels [48–50].

Thus, the instantaneous profile $s^*(z^*, t^*)$ of liquid film–soft layer interface is given by

$$s^* = a^* + S_0^* \left(1 - \frac{p^*}{2G + \lambda} \right), \quad (7)$$

where S_0^* is a prefactor that defines the initial deformation of the soft layer with the initial fluid pressure p_0^* , which will be determined later. Note that the relaxation of stresses in the soft layer is assumed to be rapid compared to the characteristic timescale of film flows, namely, the deformation of the elastic layer responds instantaneously to the hydrodynamic stresses [49].

B. Long-wave asymptotics

Before formulating a detailed asymptotic model, we first choose appropriate scaling arguments to nondimensionalize the coupled film–soft layer system. We adopt scalings as follows: the length

scale in the radial direction r^* is the unperturbed film thickness h_0^* , and that in the streamwise direction z^* is the capillary length $l_c^* = \sigma/(\rho g h_0^*)$. This choice of scales is similar to that by Craster and Matar [8] for the viscous film flows down the exterior of a rigid cylinder. Here, based on the lubrication theory, we derive the asymptotic model by assuming that the mean thickness h_0^* of the film is much smaller than its characteristic length l_c^* , namely $h_0^* \ll l_c^*$. Thus, we define a small-scale ratio $\epsilon = h_0^*/l_c^*$, which then is naturally tied to the Bond number, namely $\epsilon \equiv \text{Bo} = \rho g h_0^{*2}/\sigma$, set by the balance between the gravity and surface tension force. Note that the Bond number is small ($\text{Bo} < 0.3$) in typical surface-tension-dominated fiber-coating experiments; for instance, in the studies by Craster and Matar [8] and Duprat *et al.* [11]. Then, all the scales can be written as

$$\begin{aligned} (u^*, w^*) &= (\epsilon \mathcal{W}^* u, \mathcal{W}^* w), & (r^*, a^*, h^*, s^*, s_0^*, \mathcal{S}_0^*) &= h_0^* (r, a, h, s, s_0, \mathcal{S}_0), \\ z^* &= l_c^* z, & p^* - p_g &= \rho g l_c^* p, & t^* &= l_c^*/\mathcal{W}^* t, \end{aligned} \quad (8)$$

where $\mathcal{W}^* = \rho g h_0^{*2}/\mu$ is the characteristic streamwise velocity, given by the balance between the gravity and the viscous force. With these scales, we remove all asterisk superscripts and yield the following dimensionless governing equations:

$$u_r + \frac{u}{r} + w_z = 0, \quad (9a)$$

$$\epsilon^4 \text{Re}(u_t + uu_r + wu_z) = -p_r + \epsilon^2 \left(u_{rr} + \frac{u_r}{r} - \frac{u}{r^2} + \epsilon^2 u_{zz} \right), \quad (9b)$$

$$\epsilon^2 \text{Re}(w_t + uw_r + ww_z) = -p_z + \left(w_{rr} + \frac{w_r}{r} + \epsilon^2 w_{zz} \right) + 1, \quad (9c)$$

where $\text{Re} = \rho \mathcal{W}^* l_c^*/\mu$ is the Reynolds number, denoting the ratio of inertial to viscous forces.

The dimensionless boundary condition at the liquid film–soft layer interface $r = s(z, t)$ is

$$w = v = 0. \quad (10)$$

The dimensionless boundary conditions at the liquid film–air free surface $r = h(z, t)$ are

$$2\epsilon^2 h_z (u_r - w_z) + (1 - \epsilon^2 h_z^2)(\epsilon^2 u_z + w_r) = 0, \quad (11a)$$

$$p + \frac{2\epsilon^2}{1 + \epsilon^2 h_z^2} [h_z(\epsilon^2 u_z + w_r) - u_r - \epsilon^2 h_z^2 w_z] = \frac{1}{h(1 + \epsilon^2 h_z^2)^{1/2}} - \frac{\epsilon^2 h_{zz}}{(1 + \epsilon^2 h_z^2)^{3/2}}, \quad (11b)$$

$$h_t + wh_z = u. \quad (11c)$$

The elastohydrodynamic coupling at $r = s(z, t)$ now becomes

$$s = a + \mathcal{S}_0(1 - \mathcal{E}p), \quad (12)$$

where $\mathcal{E} = \sigma/[(2G + \lambda)h_0]$ is the elastocapillary number, defining the relative importance of the surface tension to elastic forces.

We are here primarily interested in low-Reynolds-number flows, namely, $\text{Re} = O(1)$, and also surface-tension-dominated flows, i.e., $\epsilon \equiv \text{Bo} \ll 1$, so that we can simplify the above set of governing equations by removing the inertial contributions. By further omitting the terms of $O(\epsilon^2)$ and beyond, we yield the governing equations at the leading order $O(\epsilon^0)$, in the form of

$$u_r + \frac{u}{r} + w_z = 0, \quad p_r = 0, \quad p_z = w_{rr} + \frac{w_r}{r} + 1. \quad (13)$$

The leading-order boundary conditions at $r = s(z, t)$ remain unaltered, namely, Eq. (10), and the leading-order boundary conditions at $r = h(z, t)$ become

$$w_r = 0, \quad p = \frac{1}{h} - \epsilon^2 h_{zz}. \quad (14)$$

Note that the axial curvature $\epsilon^2 h_{zz}$ is kept in spite of $O(\epsilon^2)$, which is conventionally retained in modeling of liquid films on a cylindrical geometry. This term has been shown to be the lowest-order

term that can prevent shock formation (see, for instance, the classical review by Craster and Matar [6] for more explanations). In addition, we now can yield the prefactor \mathcal{S}_0 in Eq. (12), namely,

$$\mathcal{S}_0 = \frac{s_0}{1 - \varepsilon/h_0}, \quad (15)$$

where $h_0 = a + s_0 + h_0$ is the nondimensionalized initial radius of the fluid ring, and a similar formula for \mathcal{S}_0 can also be found in the study by Bharti *et al.* [37].

By solving the governing equations and associated boundary conditions at leading order $O(\varepsilon^0)$, namely, Eqs. (10), (13), and (14), we yield the solutions of $w(z, t)$ and $p(z, t)$ at $O(\varepsilon^0)$, given by

$$w = (1 - p_z) \left[\frac{1}{4}(s^2 - r^2) + \frac{1}{2}h^2 \ln \frac{r}{s} \right], \quad (16a)$$

$$p = \frac{1}{h} - \varepsilon^2 h_{zz}. \quad (16b)$$

The term of kinematic boundary condition Eq. (11c) at the leading order, written in its conservation form results in the long-wave model equation

$$(h^2 - s^2)_t + 2Q_z = 0, \quad (17)$$

where Q denotes the local flow rate divided by 2π , given by integrating streamwise velocity w across the annular sectional area of the liquid:

$$\begin{aligned} Q &= \int_s^h wr \, dr \\ &= \frac{1}{16}(1 - p_z) \left[4h^4 \ln \frac{h}{s} - (3h^2 - s^2)(h^2 - s^2) \right], \end{aligned} \quad (18)$$

in which the instantaneous location of the soft layer surface $s(z, t)$ is given by Eq. (12).

Substituting Eqs. (18) and (12) into Eq. (17), we yield the evolution equation in the final form

$$\left(1 - \varepsilon \mathcal{S}_0 \frac{s}{h^3}\right) h_t - \varepsilon \mathcal{S}_0 \frac{s}{h} \varepsilon^2 h_{zz,t} = -\frac{1}{16h} \left[(1 - p_z) \left(4h^4 \ln \frac{h}{s} - 3h^4 + 4h^2 s^2 - s^4 \right) \right]_z. \quad (19)$$

Note that several model equations previously reported in the literature can be recovered in the corresponding limit. For instance, in the limit of $s_0 = 0$, namely, $\mathcal{S}_0 = 0$ and thus $s = a$ in Eq. (19), an analogous asymptotic model for liquid films down a rigid cylinder can be found, such as by Craster and Matar [8] and Liu *et al.* [28] that adopted similar scalings. In the limit of a rigid coating $G \rightarrow \infty$, namely, $\varepsilon \approx 0$, we can recover the same situation but for a cylinder of radius $(a + s_0)$; if, in addition, the film is taken to be thin compared to the cylinder radius, namely, $h_0/a \ll 1$ for a vanishing coated layer or $h_0/(a + s_0) \ll 1$ for a rigid coated layer, the classical thin-film equations by Roy *et al.* [51] and by Frenkel [7] can be recovered. In this work, we do not assume the small ratio between the film thickness h_0^* and the cylinder radius a^* , and therefore the derived asymptotic model, Eq. (19), is effective not only for thin liquid films where $O(h_0^*) \ll O(a^*)$, but also for thick liquid films where $O(h_0^*) \sim O(a^*)$.

Before proceeding, we first estimate the magnitudes of dimensionless parameters that are relevant for typical physical fiber-coating scenarios. Following experiments by Kliakhandler *et al.* [16], Duprat *et al.* [11], and Ji *et al.* [20], we choose a range of the cylinder radius, $a^* \in [0.1, 1]$ mm and a representative value of the unperturbed film thickness $h_0^* \approx 0.5$ mm. For the liquid film, Rhodorsil silicone oil v50 is adopted as model fluids, where at 25 °C, the density ρ , viscosity μ , and surface tension σ are around 0.963 g cm⁻³, 50 mPa s, and 20 mN m⁻¹, respectively. For the coated soft layer, the initial thickness is set as $s_0^* \in [0-0.5]$ mm, which can be achieved, for instance, by thermal gelation of normal PDMS or PAA polymers. Additionally, a wide range of shear modulus, $G \in [1, 10^5]$ Pa is considered, which can easily be adjusted by varying the mass ratio of monomers and cross-linkers in a standard experimental protocol [40]. The Poisson ratio

ν of PDMS or PAA polymer gels reported in literature ranges in [0.45–0.49] [49], and a typical value $\nu = 0.46$ is adopted. To this end, we can estimate the magnitudes of all relevant parameters: $a \in [0.2, 2]$, $s_0 \in [0, 1]$, $\text{Bo} \equiv \epsilon \approx 0.1$, $\mathcal{W}^* \approx 47 \text{ mm s}^{-1}$, $l_c^* \approx 4.4 \text{ mm}$, $\text{Re} \approx 4$, and $\epsilon \in [0, 1.5]$. Note that $\epsilon = 0$ and $\epsilon = 1.5$ indicate that the coated solid layer is extremely stiff and very soft, respectively. In this study, we are primarily interested in exploring the interplay between the cylindrical geometry and the wall softness, and therefore the influence of three key dimensionless parameters, including the cylinder radius a , coating thickness s_0 , and coating elastocapillary number ϵ , are comprehensively examined.

III. LINEAR STABILITY ANALYSIS

We begin by examining the linear stability characteristics of a liquid film system. Following the standard approach [8], we perturb the flat interface solution h_0 with an infinitesimal perturbation in the form of Fourier modes

$$h = h_0 + \zeta \exp(ikz + \omega t), \quad (20)$$

where k is the wavenumber, $\omega = \omega_r + i\omega_i \in \mathbb{C}$ represents the complex growth rate, and the amplitude of initially imposed perturbation $\zeta \ll 1$. The imaginary part ω_i divided by the wavenumber, namely $-\omega_i/k$ gives the linear phase speed c_L , and the real part ω_r quantifies the growth rate of perturbation waves. Substituting the normal decomposition, Eq. (20), into the evolution, Eq. (19), and ignoring the high-order terms in ζ leads to the general dispersion relation $\omega(k)$:

$$\omega(k) = \frac{1}{A + Bk^2} (iM_1k + M_2k^2 + iM_3k^3 + M_4k^4), \quad (21)$$

where the derivations of the coefficients M_1, M_2, M_3, M_4, A , and B are obtained with the aid of *Mathematica* and their expressions are provided in Appendix A.

A. Spatial stability analysis

Based on Eq. (21), we yield the real part $\omega_r(k)$:

$$\omega_r(k) = \frac{1}{A + Bk^2} (M_2 + M_4k^2)k^2, \quad (22)$$

where $k \in \mathbb{R}$, and the film flow is stable, marginally stable, and temporally unstable for $\omega_r < 0$, $\omega_r = 0$, and $\omega_r > 0$, respectively. Note that setting $\omega_r = 0$ gives the cutoff wavenumber, namely, $k_c = 1/(\epsilon h_0)$, which demarcates the stable and unstable regions. Surprisingly, this reveals that the cutoff mode is independent of the elasticity of the coated soft layer; it is determined solely by the average radius of the free surface h_0 , and thus by the geometric parameters of the initial film thickness h_0 , cylinder radius a , and coating thickness s_0 .

The linear growth rates ω_r for a variety of cylinder radius, wall thickness, and wall elasticity, characterized by three parameters, namely, a , s_0 , and elastocapillary number ϵ , are shown in Figs. 2(a)–2(c), respectively. For all parameter values, the free surface is unstable to the long-wave disturbance, bounded by the cutoff wavenumber $k_c = 1/(\epsilon h_0)$. As we increase the radius a of the rigid cylinder, the maximum growth rate $\omega_{r,m}$ decreases, indicating that the interface becomes more linearly stable [Fig. 2(a)]. In the fiber-coating system, the azimuthal component of curvature, $1/h$, in Eq. (16b) plays a destabilizing role [8], and thus the flow is more stable when the radius a is increased. For fixed values of $a = 0.5$, $\epsilon = 0.1$, and $\epsilon = 1$, we observe that increasing the thickness s_0 of the coated soft layer can also mitigate Rayleigh-Plateau instability, indicated by the reduced $\omega_{r,m}$ [Fig. 2(b)]. Also, the associated fastest growing mode k_m becomes smaller when s_0 increases. The observation that thicker soft coating with a same elasticity giving rise to slower growing rate is expected, as increasing s_0 will also lead to a larger apparent cylinder radius ($a + s_0$), and thus a weaker Rayleigh-Plateau instability. For the value of critical wavenumber k_c , it increases with decreasing a or s_0 , because $k_c \equiv 1/(\epsilon h_0)$ where the thickness of the flat film interface is in the form

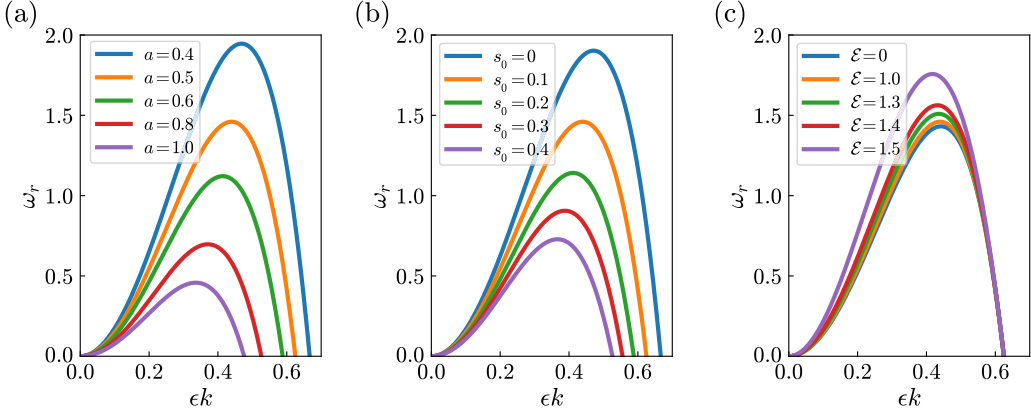


FIG. 2. Dependence of growth rate ω_r on the rescaled wavenumber ϵk predicted by linear stability analysis for (a) dimensionless radius $a = 0.4, 0.5, 0.6, 0.8,$ and 1.0 with $s_0 = 0.1$ and $\epsilon = 1$; (b) coating thickness $s_0 = 0, 0.1, 0.2, 0.3,$ and 0.4 with $a = 0.5$ and $\epsilon = 1$; and (c) elastocapillary number $\epsilon = 0, 1.0, 1.3, 1.4,$ and 1.5 with $a = 0.5$ and $s_0 = 0.1$. Other parameter: $\epsilon = 0.1$.

of $h_0 = a + s_0 + h_0$. For fixed values of $a = 0.5, \epsilon = 0.1,$ and $s_0 = 0.1,$ we find that increasing the elastocapillary number $\epsilon,$ for instance by decreasing the shear modulus G of the coated soft solid, leads to the increased $\omega_m,$ and thus a more unstable system. As expected, k_c is independent on the elastocapillary number $\epsilon,$ as shown in Fig. 2(c).

To clearly identify the impact of the soft layer on the dominant growing mode, we further calculate the maximum growth rate $\omega_{r,m}$ and the corresponding fastest growing wavenumber $k_m.$ By letting $d\omega_r/dk = 0$ in Eq. (22), we get $BM_4k^4 + 2AM_4k^2 + AM_2 = 0,$ and thus k_m is given by

$$k_m = \begin{cases} \frac{1}{\sqrt{2\epsilon h_0}}, & \text{for } s_0 = 0 \text{ or } \epsilon = 0 \\ \sqrt{-\frac{A}{B} + \sqrt{\left(\frac{A}{B}\right)^2 + \frac{1}{(\epsilon h_0)^2} \frac{A}{B}}}, & \text{for } s_0 \neq 0 \text{ and } \epsilon \neq 0. \end{cases} \quad (23)$$

The effect of elastocapillary number ϵ on the frequency k_m and the growth rate $\omega_{r,m}$ of the most unstable mode are shown in Figs. 3(a) and 3(b), respectively. For fixed values of $a = 0.5, \epsilon = 0.1,$ and $\epsilon = 0.5,$ we can observe that the frequency k_m and the growth rate $\omega_{r,m}$ of the most unstable mode decrease monotonically with increasing the coating thickness s_0 [Fig. 3(a)]. Although the presence of a soft layer gives rise to large $\omega_{r,m},$ it reduces the k_m and thus possibly increases the wavelength of the dominated surface waves [Fig. 3(b)]. In particular, k_m and $\omega_{r,m}$ change drastically as ϵ is approaching the value of $h_0,$ which is due to the discontinuity of Eq. (23), namely, S_0 in the term B (see Appendix A) will be mathematically singular as $\epsilon \rightarrow h_0.$ Note that $\epsilon < h_0$ is considered in this study, which does not cross this discontinuity. These observations from the temporal linear analysis on the linear growth rate are consistent with a recent study by Bharti *et al.* [37] for viscous films coated on a horizontally placed soft fiber. However, compared to the study by Bharti *et al.* [37], the presence of gravity can modulate the Rayleigh-Plateau instability and probably lead to sliding droplets of a constant speed [16]. This difference is characterized by the additional term, namely, the imaginary part of the dispersion relation, Eq. (21).

The imaginary part of Eq. (21) gives $\omega_i(k) = (M_1k + M_3k^3)/(A + Bk^2),$ and the linear phase speed can be calculated by

$$c_L = -\frac{M_1 + M_3k^2}{A + Bk^2}, \quad (24)$$

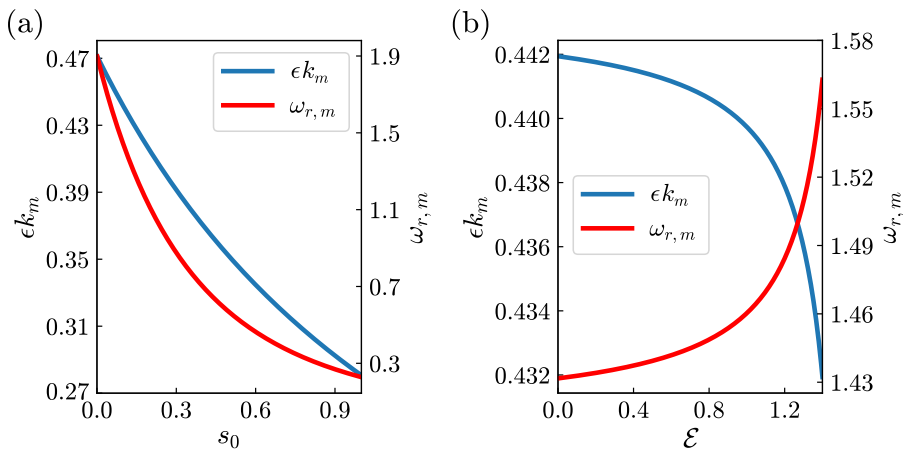


FIG. 3. Dependence of the rescaled wavenumber ϵk_m and growth rate $\omega_{r,m}$ of the most unstable mode on (a) coating thickness s_0 with $\mathcal{E} = 0.5$ and (b) elastocapillary number \mathcal{E} with $s_0 = 0.1$. Other parameters: $a = 0.5$ and $\epsilon = 0.1$.

which suggests that c_L strongly correlates to the thickness s_0 and elastocapillary number \mathcal{E} of the coated soft layer (see expressions of M_1 , M_3 , A and B in Appendix A). The impact of a , s_0 , and \mathcal{E} on the linear phase speed c_L of the free surface disturbance for given parameter values is shown in Figs. 4(a)–4(c), respectively. We note that a larger cylinder radius a gives rise to a smaller linear wave speed c_L , as shown in Fig. 4(a). As expected, for the two particular cases, i.e., the case without coating [$s_0 = 0$; the blue line in Fig. 4(b)] and the case with a rigid coating [$\mathcal{E} = 0$; the blue line in Fig. 4(c)], the linear phase speed does not change with the wavenumber k , namely, $c_L \equiv M_1$, which is independent of k [see Eq. (A1) in Appendix A]. For given nonzero values of s_0 or \mathcal{E} , the linear wave speed c_L is always increasing monotonically with the rescaled wavenumber ϵk . In addition, for a given ϵk , the coated layer gives rise to a larger c_L , suggesting that droplets travel faster on soft-layer-coated cylinders compared to those without the soft coating [Figs. 4(b) and 4(c)].

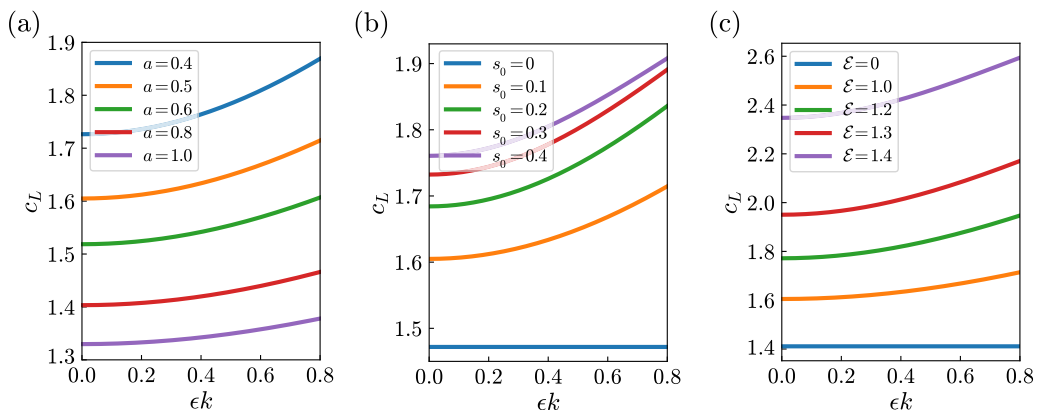


FIG. 4. Dependence of the linear phase speed c_L on the rescaled wavenumber ϵk for (a) dimensionless radius $a = 0.4, 0.5, 0.6, 0.8,$ and 1.0 with $s_0 = 0.1$ and $\mathcal{E} = 1$; (b) coating thickness $s_0 = 0, 0.1, 0.2, 0.3,$ and 0.4 with $a = 1$ and $\mathcal{E} = 1$; and (c) elastocapillary number $\mathcal{E} = 0, 1.0, 1.2, 1.3,$ and 1.4 with $a = 0.5$ and $s_0 = 0.1$. Other parameter: $\epsilon = 0.1$.

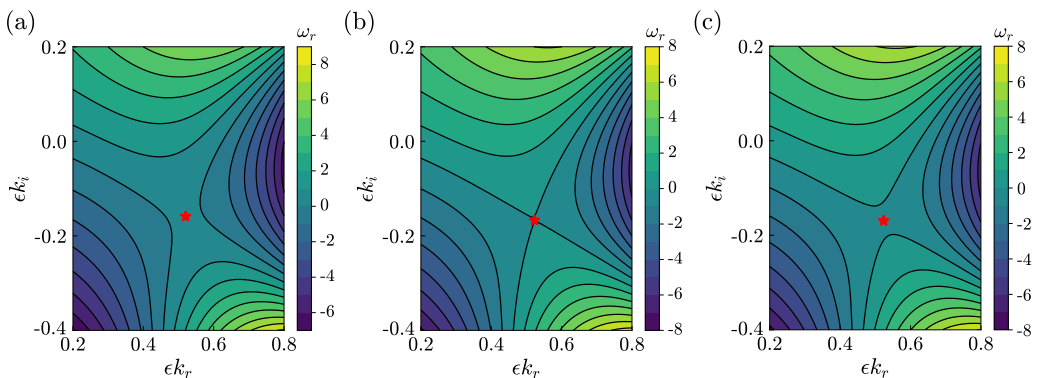


FIG. 5. Contour maps of ω_r in the rescaled complex plane $(\epsilon k_r, \epsilon k_i)$ for (a) a rigid coating $\varepsilon = 0$ where a saddle point locates at $(\epsilon k_r, \epsilon k_i) = (0.521, -0.159)$ (red star) with real growth rate $\omega_r = 0.12$; (b) a soft coating $\varepsilon = 0.45$ where a saddle point locates at $(\epsilon k_r, \epsilon k_i) = (0.523, -0.166)$ (red star) with $\omega_r = -0.002$; and (c) a soft coating $\varepsilon = 0.6$ where a saddle point locates at $(\epsilon k_r, \epsilon k_i) = (0.524, -0.169)$ (red star) with $\omega_r = -0.07$. Other parameters: $a = 0.5$, $s_0 = 0.1$, and $\epsilon = 0.1$.

B. Spatiotemporal stability analysis

Though the growth rate of the imposed sinusoidal perturbation is determined only by ω_r , the imaginary part ω_i of Eq. (21) reveals that a nonzero axial base flow, i.e., the spatial evolution of an initially local perturbation, exists. Therefore, we next examine the impact of the coated soft layer on the absolute or convective nature of the linear instabilities. Briefly, in the case of an absolutely unstable system, the initially localized disturbance will eventually invade the entire domain. In contrast, for a convectively unstable system, despite continuing to grow in time, the localized disturbance will be finally convected away from the initial location [52]. The type of convective or absolute instability can be distinguished by the most amplified wave of zero group velocity $v_g = \partial\omega/\partial k$. By applying $v_g|_{k=k_0} = 0$ to the general dispersion relation Eq. (21), we search for saddle points (k_0, ω_0) of the system, with an implicit expression for the complex wavenumber ($k = k_r + ik_i \in \mathbb{C}$):

$$iAM_1 + 2AM_2k_0 + i(3AM_3 - BM_1)k_0^2 + 4AM_4k_0^3 + iBM_3k_0^4 + 2BM_4k_0^5 = 0, \quad (25)$$

where k_0 and $\omega_0 = \omega|_{k=k_0}$ are the absolute wavenumber and the absolute wave frequency related to the zero-group velocity disturbances, respectively. In particular, the real part of ω_0 , denoted by $\omega_{0,r}$, delineates the transition between the convectively unstable and absolutely unstable: if $\omega_{0,r} > 0$, the system is absolutely unstable; if $\omega_{0,r} < 0$, it is convectively unstable. Consequently, $\omega_{0,r} = 0$ is a necessary condition at the boundary between the convectively and the absolutely unstable. Note that from Eq. (25), we can obtain three saddle points in the rescaled long-wavelength plane $(\epsilon k_r, \epsilon k_i) \in [1, -1]$, including a pure imaginary value in the upper half-plane and another two complex values in the lower half-plane. Nevertheless, the upper saddle point is spurious and does not satisfy the Briggs-Bers collision criterion. Theoretically, the saddle point that associated with an absolute-to-convective transition must be a pinch point generated by two distinct spatial branches of solutions; the two solutions are from the upper and lower half- k planes, respectively (see, e.g., Refs. [52] and [53] for a rigorous explanation). The other two saddle points are pinch points produced from two distinct branches from the upper and lower planes, and thus are physical and valid for determining the absolute or convective instability [54]. Following Ding *et al.* [29], we adopt the saddle point in the fourth quadrant to determine the absolute-to-convective transition.

Figures 5(a)–5(c) show three typical contour plots of the real part of absolute growth rate ω_r in the $(\epsilon k_r, \epsilon k_i)$ complex plane for given combinations of parameters a , s_0 , and ε , with $\epsilon = 0.1$. In the case of rigid coating, namely, $a = 0.5$, $s_0 = 0.1$, and $\varepsilon = 0$, at the saddle points

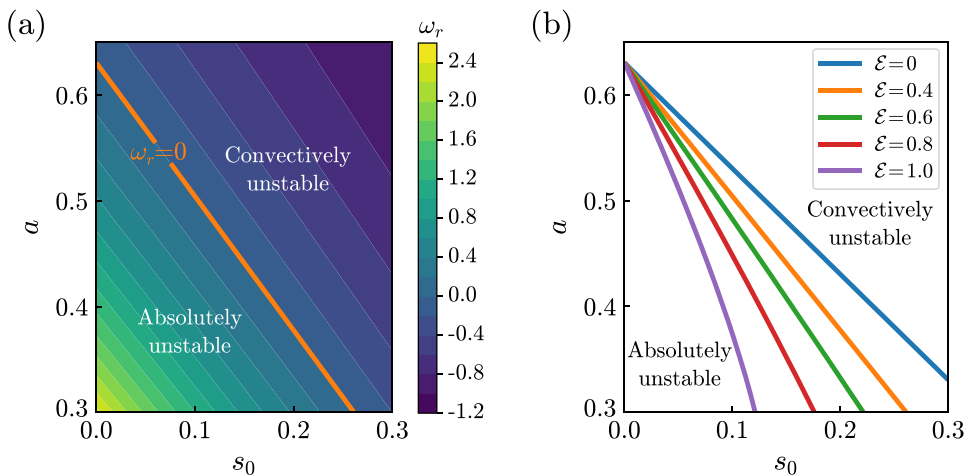


FIG. 6. Phase diagram showing the boundary between absolutely and convectively unstable regimes. (a) Contour plot of ω_r in the s_0 - a plane for $\varepsilon = 0.4$ and (b) marginal stability curves in the s_0 - a plane for $\varepsilon = 0, 0.4, 0.6, 0.8,$ and 1.0 . Other parameter: $\epsilon = 0.1$.

$\epsilon k = (0.521, -0.159)$, the real part of absolute frequency $\omega_{0,r} := 0.12 > 0$, indicating that the system is absolutely unstable [Fig. 5(a)]. As the wall softness ε is increased, pinching between spatial branches originating from the upper and lower half-planes occurs at the elastocapillary number $\varepsilon \approx 0.45$, i.e., at the saddle point $\epsilon k = (0.523, -166)$, $\omega_{0,r} := 0.002 \approx 0$, indicating that an absolute-to-convective transition is happening [Fig. 5(b)]. Notably, as we consider a soft coated layer, for instance, $\varepsilon = 0.6$, we can observe that at the saddle point $\epsilon k = (0.524, -169)$, $\omega_{0,r} := -0.07 < 0$, indicating that the flow now becomes convectively unstable [Fig. 5(c)]. Thus, for every parameter combination related to the linearly unstable regime, there is a critical elastocapillary number ε_c corresponding to the absolute-to-convective transition. For instance, $\varepsilon_c \approx 0.45$ for $a = 0.5$, $s_0 = 0.1$, and $\epsilon = 0.1$. As a consequence, there exists a parameter space of s_0 and/or ε for which the advection of the waves always dominates over the Rayleigh-Plateau mechanism, and the instability is convective.

However, exploring the critical values of ε and s_0 analytically is a challenging task, as we cannot directly obtain an explicit formula for ε_c in terms of a , ϵ , and s_0 or $s_{0,c}$ in terms of a , ϵ , and ε from Eq. (25). Therefore, we numerically capture the dependence of critical values of ε , s_0 , and a on the other parameters. Figure 6(a) shows a typical contour plot for ω_r in the s_0 - a plane for the case of $\varepsilon = 0.4$. For the combination of the two parameters (s_0, a) above the marginal stability curve $\omega_r = 0$, the flow is absolutely unstable, while it is convectively unstable if (s_0, a) is below the curve. The marginal stability curves of the s_0 - a plane for various elastocapillary numbers, including $\varepsilon = 0, 0.4, 0.6, 0.8,$ and 1 are further summarized into Fig. 6(b). Apparently, by increasing ε from 0 to 1, we observe that the absolutely unstable regime shrinks significantly in the s_0 - a plane, suggesting that the wall softness can suppress the absolute instability. In previous experiments by Duprat *et al.* [11] for viscous films falling down a rigid fiber, convective (absolute) instability of the flows is observed when the film is very thin (thick) compared to the fiber radius. In a recent theoretical study by Ding *et al.* [29], they further showed that the thermal Marangoni effect induced by wall heating (cooling) can also trigger the film flows from being convective (absolute) to being absolute (convective) instability. Our observations suggest that coating the cylindrical surface with a thin layer of soft solids, such as gelled PDMS polymers, provides another possibility to trigger a transition in the film flows from absolutely unstable to convectively unstable (Fig. 6).

IV. TRANSIENT NUMERICAL SIMULATIONS

To validate the linear analysis results and to further study the nonlinear development of the instabilities, we next perform transient numerical solutions of Eq. (19) to reveal both temporal and spatiotemporal dynamics of the film system. Before performing the transient simulations, we follow the canonical methodology by Benney [55] to approximate the highly coupled spatiotemporal term $h_{zz,t}$ in Eq. (19), yielding the following evolution equation:

$$f_1 h_t + \epsilon^2 f_2 \left(\frac{f_{3,z}}{f_1} \right)_{zz} = f_{3,z}, \quad (26)$$

with

$$f_1 = \left(1 - \epsilon \mathcal{S}_0 \frac{s}{h^3} \right) h, \quad f_2 = -\epsilon \mathcal{S}_0 s, \\ f_3 = -\frac{1}{16} (1 - p_z) \left(4h^4 \ln \frac{h}{s} - 3h^4 + 4h^2 s^2 - s^4 \right),$$

where the detailed derivation is given in Appendix B. Based on this simplification, we carry out the numerical simulations of Eq. (26) in a periodic space domain $z \in [0, L]$, where L is the length of the computational domain. The pseudospectral algorithm is applied, namely, spatial derivatives and strongly nonlinear terms are computed in Fourier space and physical space, respectively. The Fourier series used to discretize the spatial domain [56] is in the form of

$$h(z, t) = \sum_{m=-N/2}^{N/2} \hat{H}_m(t) \exp\left(im \frac{2\pi}{L} z \right), \quad (27)$$

where $\hat{H}_m(t)$ and N are the time-dependent Fourier coefficients and the number of Fourier modes, respectively. Depending on the length of the computational domain, we adopt different Fourier modes $N \in [128, 512]$. For the time marching, the backward differentiation formula (BDF) method for stiff problems is implemented with a relative error set below 10^{-8} of the solutions [57].

A. Temporally nonlinear evolution

We first perform transient simulations of Eq. (26) to examine the temporally nonlinear evolution from a perturbed initial state in a short computational domain. The initial condition in the form of a simple harmonic disturbance is superimposed on the flat interface, given by

$$h(z, 0) = h_0 + 0.1 \cos(k_m z), \quad (28)$$

where k_m is the most unstable mode, given by Eq. (23), the computational domain is set as $L = 2\pi/k_m$, and the number of Fourier modes is $N = 128$. The saturated states of the free interface h and the associated deformation of the soft layer ($s - a$) from the numerical solutions for three elastocapillary numbers, including $\epsilon = 0, 0.5$, and 0.8 are shown in Figs. 7(a)–7(c), respectively. Other parameters are fixed: $a = 0.5$, $s_0 = 0.1$, and $\epsilon = 0.1$. For all three cases, as $a < h_0$, the isolated sliding droplets are well formed, resonating with the experimental observations in the regime of thick liquid films by Kliakhandler *et al.* [16] and Craster and Matar [8]. As an example, in a typical experiment by Craster and Matar [8], the ratio of initial radius to that of the fiber is 0.25 and $\epsilon = 0.1$, a well-defined droplet profile can be observed. For our case, $\epsilon = 0.1$ and the ratio $a/(a + s_0 + h_0) = 0.31$, which is close to that experiment (0.25), suggesting a thick film regime. Thus, the isolated sliding droplets can be clearly seen. Notably, when the coated solid layer becomes softer, from $\epsilon = 0$ to 0.8 , the deformation of the layer becomes significant. In particular, as expected from Eq. (12), the deformation is particularly visible in the location with the strongest capillary pressure p_{\max} [see the red star marked in Fig. 7(c)].

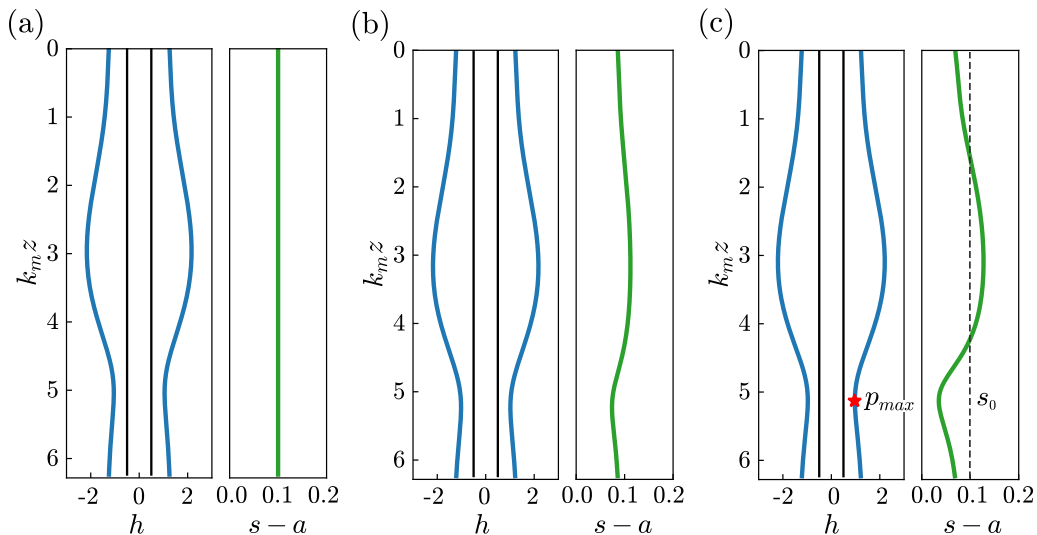


FIG. 7. Saturated states of the free interface for different coating elasticity: (a) $\varepsilon = 0$, (b) $\varepsilon = 0.5$, and (c) $\varepsilon = 0.8$. Left panels: profiles of the liquid film. Right panels: profiles of the soft layer. Other parameters: $a = 0.5$, $s_0 = 0.1$, and $\epsilon = 0.1$.

To clearly observe the impact of wall elasticity, we further calculate the temporal evolution of maximal height h_{max} of the film interface and the absolute maximal deformation of soft layer in the form of $|s - a - s_0|_{max}$ for various elastocapillary numbers $\varepsilon = 0, 0.5, 0.6, 0.7$, and 0.8 , as shown in Figs. 8(a) and 8(b), respectively. Other parameters are the same as those in Fig. 7. Apparently, compared to those with a rigid coating ($\varepsilon = 0$), the presence of a soft coated layer leads to larger magnitudes h_{max} of sliding droplets as well as larger maximal deformation $|s - a - s_0|_{max}$ of the coated layer. These observations indicate that wall elasticity can promote the growth of Rayleigh-Plateau instability, agreeing well with the predications by the linear stability analysis [see Fig. 2(c)]. In particular, for all parameter values, the perturbation grows rapidly at the early stage, and then

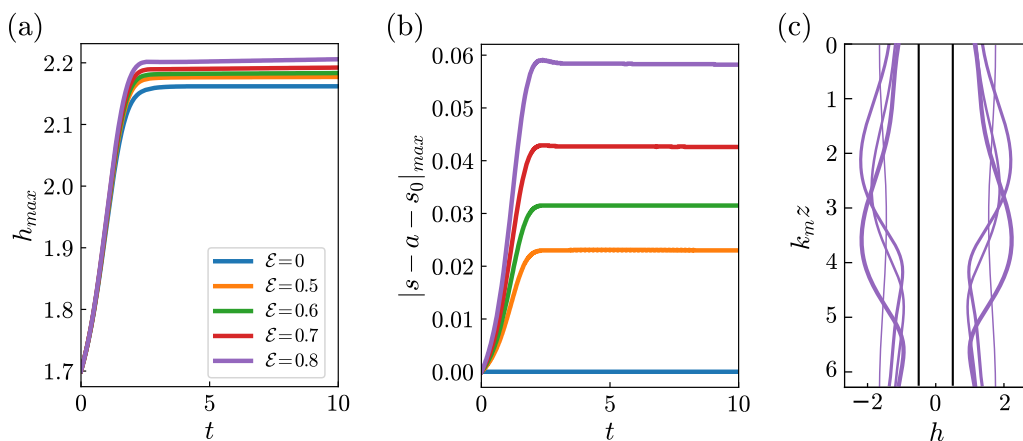


FIG. 8. Temporal growth of the perturbations for various ε : (a) The maximal height h_{max} of the interface and (b) the absolute value of maximal deformation $|s - a - s_0|_{max}$ of the soft layer as a function of t . (c) The time sequence of the free surface for $\varepsilon = 0.8$ at $t = 0, 1.5, 3$, and 5 illustrated from thin to thick purple lines. Other parameters: $a = 0.5$, $s_0 = 0.1$, and $\epsilon = 0.1$.

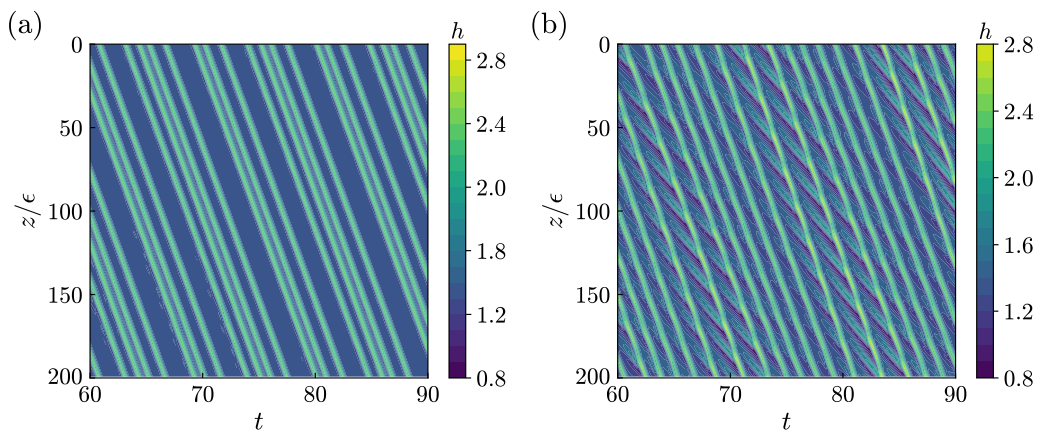


FIG. 9. Spatiotemporal diagrams illustrating the dynamics of the free surface $h(z, t)$ for (a) $\varepsilon = 0$ and (b) $\varepsilon = 0.6$. The bright and dark shading indicate the elevated and depressed regions, respectively. Other parameters: $a = 0.5$, $s_0 = 0.1$, $\epsilon = 0.1$, and $L = 20$.

gradually reaches a plateau due to the nonlinear saturation at the later stage. This can be shown, as an example, by illustrating the time-sequence evolution of free surface $h(z, t)$ corresponding to the case of $\varepsilon = 0.5$ at $t = 0, 1.5, 3$, and 5 [see Fig. 8(c)].

We examine the transient numerical simulations of Eq. (26) again, but this time using a relatively large computational domain $L = 20$ with a Fourier mode $N = 256$ to understand the complex nonlinear dynamics of liquid film. Typically, the initial condition $h(z, 0) = h_0 + 0.1 \cos(\frac{2\pi}{L}z)$ evolves through an initial transient, during which the wavelength of the maximum growth rate $\omega_{r,m}$ is selected by the model and gradually dominates the free surface flow. This is followed by a later time evolution where the instabilities reach near constant amplitude. Figures 9(a) and 9(b) show the spatiotemporal evolution of film interfaces $h(z, t)$ for two typical scenarios $\varepsilon = 0$ and $\varepsilon = 0.6$ with given $a = 0.5$, $s_0 = 0.1$, and $\epsilon = 0.1$. In the case of a rigid coating ($\varepsilon = 0$), we observe that the drop train is highly organized, where the drop shape, sliding speed as well as the spacing between droplets do not change with time, as shown in Fig. 9(a). This phenomenon was also reported in several previous experimental studies, for instance, in “(b)” or “Rayleigh-Plateau” regime of experiments by Kalliadasis and Chang [15], Craster and Matar [8], and Ji *et al.* [20] for films falling down rigid cylinders. By contrast, when the coated layer becomes softer where $\varepsilon = 0.6$, sliding droplets with large amplitudes coalesce with preceding slower moving droplets of relatively small amplitudes [see Fig. 9(b) and the coalescence event of two distinct droplets in Fig. 11 of Appendix C]. The oscillation of the film surface is also observed, which is caused by the competition between coalescence of droplets and their transition to smaller scales, as shown in Fig. 9(b), which is similar to the “(c)” or “convective” regime of experiments in the case of rigid cylinders by Kalliadasis *et al.* [8,15,20]. This observation means increasing the wall softness by increasing elastocapillary number ε leads to the formation of more unstable sliding-droplet systems. Nevertheless, similar to the results observed in the case of a short domain, in both scenarios, during the early stages, waves grow in amplitude. At the later stages, the nonlinearities in the model cause the saturation of wave growth, resulting in wave trains propagating down the cylinder. Despite these waves interacting with one another, they eventually maintain a mostly steady shape.

B. Spatiotemporally nonlinear evolution

Next, we perform a localized disturbance-response analysis with transient simulations of Eq. (26) to examine its spatiotemporal dynamics. To this end, a localized disturbance is seeded near the inlet

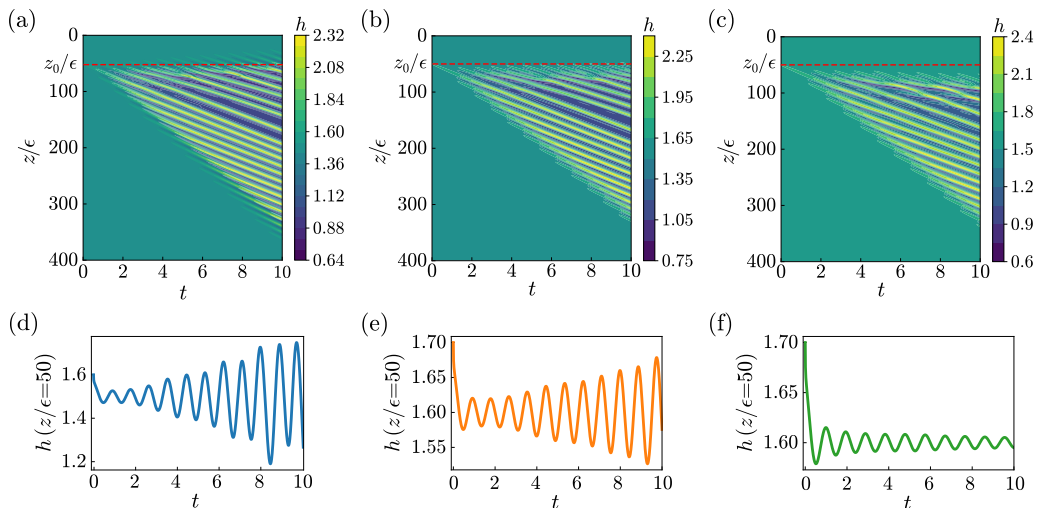


FIG. 10. Spatiotemporal diagrams illustrating the evolution of a local disturbance for (a) $s_0 = 0$ and $\varepsilon = 0$ for an absolutely unstable flow, (b) $s_0 = 0.1$ and $\varepsilon = 0$ for a weak absolutely unstable flow, and (c) $s_0 = 0.1$ and $\varepsilon = 0.6$ for a convectively unstable flow. (d)–(f) The temporal evolution of the disturbance at its origin $z/\varepsilon := z_0/\varepsilon = 50$, corresponding to the red dashed lines in (a), (b), and (c), respectively. Other parameters: $a = 0.5$, $\varepsilon = 0.1$, and $L = 40$.

region ($z = z_0$) into the initially flat film in a large computational domain $L = 40$, given by

$$h(z, 0) = h_0 + 0.1 \exp\left[-\frac{1}{2}(z - z_0)^2\right], \quad (29)$$

where the inlet location $z_0 = 5$ and a large Fourier mode $N = 512$ are employed. Conventionally, for a convective instability, both the leading and receding front velocities (V_f^\pm) of the localized disturbance are positive, and thus the instability will be convected away from the initial location. By contrast, for an absolute instability, a positive (+) leading front and a negative (–) receding front are both present, leading to the contamination of an entire domain by the initial disturbance. This concept can be clearly seen by illustrating the spatiotemporal diagram of the wave packet emerging from the initial localized excitation.

We examine the following three typical cases: (i) $s_0 = 0$ and $\varepsilon = 0$, (ii) $s_0 = 0.1$ and $\varepsilon = 0$, and (iii) $s_0 = 0.1$ and $\varepsilon = 0.6$, with all three cases given $a = 0.5$ and $\varepsilon = 0.1$. Successive snapshots showing the evolution of the free surface, in the form of spatiotemporal diagrams corresponding to the three cases are illustrated in Figs. 10(a)–10(c), respectively. In particular, to avoid the fouling of perturbations at the upstream, we terminate the calculation before the perturbation periodically reenters the computational domain from upstream. For case (i) that is without the coated layer ($s_0 = 0$), the base flow is relatively small and the initial perturbation gradually invades the entire computational domain, indicating that the flow exhibits an absolute instability [see Fig. 10(a)]. In this case, the spatially growing modes play a secondary role as they are eventually swamped by the time-dependent growth at any fixed location along the cylinder, and in particular at $z/\varepsilon = 50$. This can also be clearly seen by plotting the amplitude of the disturbance h as a function of time t at its original location $z/\varepsilon = 50$ [see the horizontal dashed line in Fig. 10(a)], of which amplitude is rapidly amplified with time [Fig. 10(d)]. In the presence of a rigid coating ($s_0 = 0.1$, $\varepsilon = 0$), the sweeping of base flow becomes large, leading to a relatively weak absolute flow [Figs. 10(b) and 10(d)]. This result is consistent with the experimental observation by Duprat *et al.* [11] for the case of films falling down a rigid fiber, namely, increasing the fiber radius is capable of attenuating the absolute instability, and even leads to a transition to the regime of convective instability. However,

as the coated layer becomes soft ($s_0 = 0.1$, $\varepsilon = 0.6$), which is larger than the critical elastocapillary number $\varepsilon_c \approx 0.45$ predicted by spatiotemporal linear analysis, the base flow now is strong enough to carry the perturbation downstream. As shown in Fig. 10(c), the noise is gradually flowing away from the initial location of the imposed pulse, indicating the flow now transits from an absolute instability into a convective instability. As a result, the amplitude of the initial disturbance at $z/\varepsilon = 50$ is gradually damped with time [Fig. 10(f)]. In addition, compared to the elastocapillary effect due to the coating softness, we note that the geometric effect caused by the coating thickness seems to be more pronounced [see Figs. 10(d)–10(f)]. Though such disturbances are local in space, they can globally alter the pressure p^* and thus the deformation δ^* . Note that we here assume that the deformation of the elastic layer responds instantaneously to the flow-imposed stresses [49]. To briefly conclude, the spatiotemporal solutions from transient simulations further show that the absolute instability can transition to the convective nature when a layer of soft solid is coated on the cylinder, agreeing well with the predication of spatiotemporal stability analysis [Figs. 5(a) and 5(c)].

V. CONCLUSIONS

In summary, we have investigated the Rayleigh-Plateau instability of a gravity-driven viscous liquid film down the exterior surface of a soft-layer-coated cylinder. By incorporating a model Winkler elastic response into the long-wave asymptotic theory, we construct a model equation describing the spatiotemporal dynamics of the coupled liquid film–soft layer–rigid cylinder system. Based on the model, the impact of the rigid cylinder radius, coating thickness, and coating elasticity on both the linear and the nonlinear stabilities are systematically examined. Temporal stability analysis shows that the coated soft layer plays a dual role for other given factors: wall elasticity acts as a destabilizing factor, giving rise to large deformations of both film interface and soft surface. Nevertheless, due to the geometrical effect, coating a softer layer is equivalent to increasing cylinder radius, which can mitigate the Rayleigh-Plateau instability. By contrast, compared to the rigid case, both the coating elasticity and the thickness can lead to a stronger linear phase speed. We further examine the spatiotemporal stabilities of the free surface flows, and demonstrate that wall elasticity can trigger the film flows from an absolutely unstable to a convectively unstable state. Numerical solutions of the nonlinear evolution equation further confirm the results from linear stability analysis, revealing the strongly nonlinear effect of wall elasticity, namely, leading to strong coalescence events of faster, larger sliding droplets with preceding slower, smaller sliding ones down the cylinder.

Our studies adopt a similar long-wave model that was derived for liquid film flows down the exterior surface of a rigid cylinder by Craster and Matar [8]. This classical model was further experimentally validated by Smolka *et al.* [58] to be effective in describing the linear stability of such flows at low to moderate Reynolds number. However, to extend this study into film flows, the axial viscous diffusion of high-viscosity fluids and/or the inertia of low-viscosity fluids need be taken into consideration. Then, we may resort to higher-order long-wave models, such as the weighted-residual integral-boundary-layer formalism that was developed by Ruyer-Quil *et al.* [10]. In addition, we here consider that the soft layer is thin and purely elastic, which can also be extended to more complicated situations, such as the case of a thick coated layer [50], as well as viscoelastic, viscoplastic, and even poroelastic soft solid materials [39]. Furthermore, the liquid films can also be the non-Newtonian fluids, for instance, by incorporating the Oldroyd-B model [59,60]. It is worth noting that the profiles of liquid films might be converging to a stable traveling wave solution [see Fig. 7(c)], which is beyond the current study. To this end, the future work may involve these characteristics. As a final remark, we would like to note that our model can also be applicable for including the slip boundary condition, intermolecular forces, and/or nonisothermal effect. The inclusion of those effects may have important implications for recently emerging applications, for instance, the collection of fogs into fresh water on special wettable cylindrical surfaces [61] as well as directional liquid transport on flexible microfluidic-derived microfibers [62].

ACKNOWLEDGMENTS

We thank the anonymous referees for their constructive and valuable comments. Z.D. and J.C. acknowledge the National Natural Science Foundation of China (Grants No. 12102109 and No. 52125603). L.Z. acknowledges the partial support from the Singapore Ministry of Education Academic Research Fund Tier 2 grant (Grant No. MOE-T2EP50122-0015). Y.C. acknowledges the Fundamental Research Funds for the Central Universities (Grants No. AUGA2160100324 and No. AUGA2160503123).

APPENDIX A: COEFFICIENTS OF THE EVOLUTION EQUATION

The coefficients in the general dispersion relation, namely, Eq. (21), are listed as follows:

$$M_1 = -\left[\hbar_0^2 \ln \frac{\hbar_0}{a+s_0} - \frac{\hbar_0^2}{2} + \frac{1}{2}(a+s_0)^2 - \frac{\mathcal{E}\mathcal{S}_0}{16} \left(\frac{4\hbar_0}{a+s_0} \right) - \frac{8}{\hbar_0}(a+s_0) + \frac{4}{\hbar_0^3}(a+s_0)^3 \right], \quad (\text{A1})$$

$$M_2 = \left[\frac{\hbar_0}{4} \ln \frac{\hbar_0}{a+s_0} - \frac{3\hbar_0}{16} + \frac{1}{4\hbar_0}(a+s_0)^2 - \frac{1}{16\hbar_0^3}(a+s_0)^4 \right], \quad (\text{A2})$$

$$M_3 = \frac{\epsilon^2 \mathcal{E}\mathcal{S}_0}{16} \left[-\frac{4\hbar_0^3}{a+s_0} + 8\hbar_0(a+s_0) - \frac{4(a+s_0)^3}{\hbar_0} \right], \quad (\text{A3})$$

$$M_4 = -\epsilon^2 \hbar_0^2 \left[\frac{\hbar_0}{4} \ln \frac{\hbar_0}{a+s_0} - \frac{3\hbar_0}{16} + \frac{1}{4\hbar_0}(a+s_0)^2 - \frac{1}{16\hbar_0^3}(a+s_0)^4 \right], \quad (\text{A4})$$

$$A = 1 - \frac{\mathcal{E}\mathcal{S}_0}{\hbar_0^3} \left(a + \mathcal{S}_0 - \frac{\mathcal{E}\mathcal{S}_0}{\hbar_0} \right), \quad B = \frac{\mathcal{E}\mathcal{S}_0}{\hbar_0} \left(a + \mathcal{S}_0 - \frac{\mathcal{E}\mathcal{S}_0}{\hbar_0} \right) \epsilon^2. \quad (\text{A5})$$

APPENDIX B: ELIMINATION OF THE COUPLED TERM $h_{zz,t}$

The highly coupled spatiotemporal term of $h_{zz,t}$ in the evolution Eq. (19) can be approximated as follows. We first rewrite Eq. (19) in the form of

$$f_1 h_t + \epsilon^2 f_2 h_{zz,t} = f_{3,z}, \quad (\text{B1})$$

where

$$f_1 = \left(1 - \mathcal{E}\mathcal{S}_0 \frac{s}{\hbar^3} \right) h, \quad f_2 = -\mathcal{E}\mathcal{S}_0 s,$$

$$f_3 = -\frac{1}{16}(1-p_z) \left(4h^4 \ln \frac{h}{s} - 3h^4 + 4h^2 s^2 - s^4 \right).$$

Divided by f_1 in both sides in Eq. (B1) gives

$$h_t = \frac{f_{3,z}}{f_1} - \epsilon^2 \frac{f_2}{f_1} h_{zz,t} = \frac{f_{3,z}}{f_1} + O(\epsilon^2). \quad (\text{B2})$$

Then, we obtain the term $\epsilon^2 h_{zz,t}$:

$$\epsilon^2 h_{zz,t} = \epsilon^2 \left[\frac{f_{3,z}}{f_1} + O(\epsilon^2) \right]_{zz} = \epsilon^2 \left(\frac{f_{3,z}}{f_1} \right)_{zz} + O(\epsilon^4) \approx \epsilon^2 \left(\frac{f_{3,z}}{f_1} \right)_{zz}. \quad (\text{B3})$$

Substituting Eq. (B3) into Eq. (B1), we eventually eliminate $h_{zz,t}$ and yield the following simplified evolution equation:

$$f_1 h_t + \epsilon^2 f_2 \left(\frac{f_{3,z}}{f_1} \right)_{zz} = f_{3,z}. \quad (\text{B4})$$

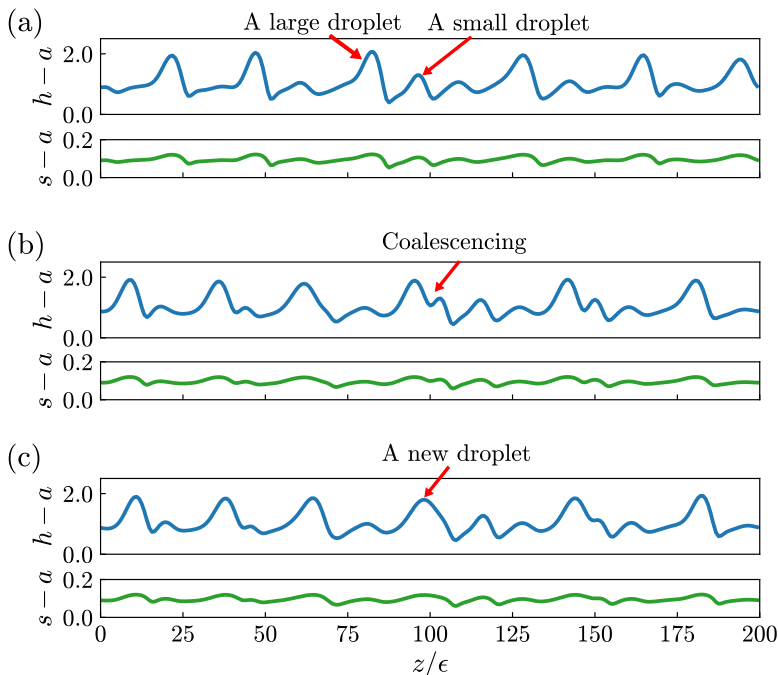


FIG. 11. Successive snapshots illustrating profiles of the free surface ($h - a$) and solid deformation ($s - a$) for $\varepsilon = 0.6$ at (a) $t = 65$, (b) $t = 65.8$, and (c) $t = 65.9$. A typical coalescence event of a large droplet with a preceding small droplet is marked. Other parameters: $a = 0.5$, $s_0 = 0.1$, $\varepsilon = 0.1$, and $L = 20$.

APPENDIX C: COALESCENCE EVENT OF SLIDING DROPLETS

The successive snapshots of surface profiles ($h - a$) and the deformation of the soft solid ($s - a$) for $\varepsilon = 0.6$ at $t = 65$, 65.8 , and 65.9 are shown in Figs. 11(a)–11(c), respectively. A typical coalescence event of a droplet with larger amplitude with a preceding slower moving droplet of relatively small amplitude can be clearly observed.

-
- [1] D. Quéré, Fluid coating on a fiber, *Annu. Rev. Fluid Mech.* **31**, 347 (1999).
 - [2] Z. Zeng, A. Sadeghpour, and Y. S. Ju, Thermohydraulic characteristics of a multi-string direct-contact heat exchanger, *Int. J. Heat Mass Transfer* **126**, 536 (2018).
 - [3] A. Sadeghpour, Z. Zeng, H. Ji, N. Dehdari Ebrahimi, A. Bertozzi, and Y. Ju, Water vapor capturing using an array of traveling liquid beads for desalination and water treatment, *Sci. Adv.* **5**, eaav7662 (2019).
 - [4] L. Rayleigh, On the instability of jets, *Proc. London Math. Soc.* **s1-10**, 4 (1878).
 - [5] J. Eggers and E. Villermaux, Physics of liquid jets, *Rep. Prog. Phys.* **71**, 036601 (2008).
 - [6] R. Craster and O. Matar, Dynamics and stability of thin liquid films, *Rev. Mod. Phys.* **81**, 1131 (2009).
 - [7] A. Frenkel, Nonlinear theory of strongly undulating thin films flowing down vertical cylinders, *Europhys. Lett.* **18**, 583 (1992).
 - [8] R. Craster and O. Matar, On viscous beads flowing down a vertical fibre, *J. Fluid Mech.* **553**, 85 (2006).
 - [9] G. M. Sisoiev, R. V. Craster, O. K. Matar, and S. V. Gerasimov, Film flow down a fibre at moderate flow rates, *Chem. Eng. Sci.* **61**, 7279 (2006).
 - [10] C. Ruyer-Quil, P. Trevelyan, F. Giorgiutti-Dauphiné, C. Duprat, and S. Kalliadasis, Modelling film flows down a fibre, *J. Fluid Mech.* **603**, 431 (2008).

- [11] C. Duprat, C. Ruyer-Quil, S. Kalliadasis, and F. Giorgiutti-Dauphiné, Absolute and convective instabilities of a viscous film flowing down a vertical fiber, *Phys. Rev. Lett.* **98**, 244502 (2007).
- [12] H. Ji, C. Falcon, E. Sedighi, A. Sadeghpour, Y. S. Ju, and A. L. Bertozzi, Thermally-driven coalescence in thin liquid film flowing down a fibre, *J. Fluid Mech.* **916**, A19 (2021).
- [13] S. L. Goren, The instability of an annular thread of fluid, *J. Fluid Mech.* **12**, 309 (1962).
- [14] Y. Y. Trifonov, Steady-state traveling waves on the surface of a viscous liquid film falling down on vertical wires and tubes, *AIChE J.* **38**, 821 (1992).
- [15] S. Kalliadasis and H.-C. Chang, Drop formation during coating of vertical fibres, *J. Fluid Mech.* **261**, 135 (1994).
- [16] I. Kliakhandler, S. H. Davis, and S. Bankoff, Viscous beads on vertical fibre, *J. Fluid Mech.* **429**, 381 (2001).
- [17] B. Kim, H. Ji, A. L. Bertozzi, A. Sadeghpour, and Y. S. Ju, A positivity-preserving numerical method for a thin liquid film on a vertical cylindrical fiber, *J. Comput. Phys.* **496**, 112560 (2024).
- [18] S. Biswal, H. Ji, K. Elamvazhuthi, and A. L. Bertozzi, Optimal boundary control of a model thin-film fiber coating model. *Physica D (Amsterdam, Neth.)* **457**, 133942 (2024).
- [19] D. Halpern and H.-H. Wei, Slip-enhanced drop formation in a liquid falling down a vertical fibre, *J. Fluid Mech.* **820**, 42 (2017).
- [20] H. Ji, C. Falcon, A. Sadeghpour, Z. Zeng, Y. Ju, and A. Bertozzi, Dynamics of thin liquid films on vertical cylindrical fibres, *J. Fluid Mech.* **865**, 303 (2019).
- [21] L. Yu and J. Hinch, The velocity of ‘large’ viscous drops falling on a coated vertical fibre, *J. Fluid Mech.* **737**, 232 (2013).
- [22] D. Quéré, Thin films flowing on vertical fibers, *Europhys. Lett.* **13**, 721 (1990).
- [23] Z. Ding and T. N. Wong, Three-dimensional dynamics of thin liquid films on vertical cylinders with Marangoni effect, *Phys. Fluids* **29**, 011701 (2017).
- [24] Y. Chao, Y. Lu, and H. Yuan, On reactive thin liquid films falling down a vertical cylinder, *Int. J. Heat Mass Transfer* **147**, 118942 (2020).
- [25] C. T. Gabbard and J. B. Bostwick, Bead-on-fibre morphology in shear-thinning flow, *J. Fluid Mech.* **961**, A14 (2023).
- [26] M. Rietz, B. Scheid, F. Gallaire, N. Kofman, R. Kneer, and W. Rohlf, Dynamics of falling films on the outside of a vertical rotating cylinder: Waves, rivulets and dripping transitions, *J. Fluid Mech.* **832**, 189 (2017).
- [27] S. Eghbali, L. Keiser, E. Boujo, and F. Gallaire, Whirling instability of an eccentric coated fibre, *J. Fluid Mech.* **952**, A33 (2022).
- [28] R. Liu, Z. Ding, and Z. Zhu, Thermocapillary effect on the absolute and convective instabilities of film flows down a fibre, *Int. J. Heat Mass Transfer* **112**, 918 (2017).
- [29] Z. Ding, R. Liu, T. N. Wong, and C. Yang, Absolute instability induced by Marangoni effect in thin liquid film flows on vertical cylindrical surfaces, *Chem. Eng. Sci.* **177**, 261 (2018).
- [30] D. Halpern and J. Grotberg, Fluid-elastic instabilities of liquid-lined flexible tubes, *J. Fluid Mech.* **244**, 615 (1992).
- [31] Z.-Q. Zhou, J. Peng, Y.-J. Zhang, and W.-L. Zhuge, Viscoelastic liquid film flowing down a flexible tube, *J. Fluid Mech.* **802**, 583 (2016).
- [32] O. K. Matar, R. V. Craster, and S. Kumar, Falling films on flexible inclines, *Phys. Rev. E* **76**, 056301 (2007).
- [33] Y. Chao and Z. Ding, Thermocapillary thin-film flows on a compliant substrate, *Phys. Rev. E* **99**, 043101 (2019).
- [34] J. P. Alexander, T. L. Kirk, and D. T. Papageorgiou, Stability of falling liquid films on flexible substrates, *J. Fluid Mech.* **900**, A40 (2020).
- [35] B. Jia and Y. Jian, Stability of a liquid film on inclined flexible substrates: Effect of the spontaneous odd viscosity, *Phys. Rev. E* **108**, 045104 (2023).
- [36] S. Chattopadhyay, A. S. Desai, A. K. Gaonkar, and A. Mukhopadhyay, Role of odd viscosity on falling films over compliant substrates, *Phys. Rev. Fluids* **8**, 064003 (2023).

- [37] B. Bharti, A. Carlson, T. S. Chan, and T. Salez, Plateau-Rayleigh instability of a viscous film on a soft fiber, *Europhys. Lett.* **145**, 67001 (2024).
- [38] B. Andreotti and J. H. Snoeijer, Statics and dynamics of soft wetting, *Annu. Rev. Fluid Mech.* **52**, 285 (2020).
- [39] B. Rallabandi, Fluid-elastic interactions near contact at low Reynolds number, *Annu. Rev. Fluid Mech.* **56**, 491 (2024).
- [40] H. Jeon, Y. Chao, and S. Karpitschka, Moving wetting ridges on ultrasoft gels, *Phys. Rev. E* **108**, 024611 (2023).
- [41] R. W. Style, Y. Che, S. J. Park, B. M. Weon, J. H. Je, C. Hyland, G. K. German, M. P. Power, L. A. Wilen, J. S. Wettlaufer, and E. R. Dufresne, Patterning droplets with durotaxis, *Proc. Natl. Acad. Sci. USA* **110**, 12541 (2013).
- [42] B. Saintyves, T. Jules, T. Salez, and L. Mahadevan, Self-sustained lift and low friction via soft lubrication, *Proc. Natl. Acad. Sci. USA* **113**, 5847 (2016).
- [43] J. M. Skotheim and L. Mahadevan, Soft lubrication, *Phys. Rev. Lett.* **92**, 245509 (2004).
- [44] K. L. Johnson and K. L. Johnson, *Contact Mechanics* (Cambridge University Press, Cambridge, 1987).
- [45] J. Skotheim and L. Mahadevan, Soft lubrication: The elastohydrodynamics of nonconforming and conforming contacts, *Phys. Fluids* **17**, 092101 (2005).
- [46] J. Urzay, S. G. Llewellyn Smith, and B. J. Glover, The elastohydrodynamic force on a sphere near a soft wall, *Phys. Fluids* **19**, 103106 (2007).
- [47] T. G. Chandler and D. Vella, Validity of Winkler's mattress model for thin elastomeric layers: Beyond Poisson's ratio, *Proc. R. Soc. A* **476**, 20200551 (2020).
- [48] B. Rallabandi, B. Saintyves, T. Jules, T. Salez, C. Schönecker, L. Mahadevan, and H. A. Stone, Rotation of an immersed cylinder sliding near a thin elastic coating, *Phys. Rev. Fluids* **2**, 074102 (2017).
- [49] B. Saintyves, B. Rallabandi, T. Jules, J. Ault, T. Salez, C. Schönecker, H. A. Stone, and L. Mahadevan, Rotation of a submerged finite cylinder moving down a soft incline, *Soft Matter* **16**, 4000 (2020).
- [50] M. H. Essink, A. Pandey, S. Karpitschka, C. H. Venner, and J. H. Snoeijer, Regimes of soft lubrication, *J. Fluid Mech.* **915**, A49 (2021).
- [51] R. V. Roy, A. Roberts, and M. Simpson, A lubrication model of coating flows over a curved substrate in space, *J. Fluid Mech.* **454**, 235 (2002).
- [52] P. Huerre and P. A. Monkewitz, Local and global instabilities in spatially developing flows, *Annu. Rev. Fluid Mech.* **22**, 473 (1990).
- [53] R. J. Briggs, *Electron-Stream Interaction with Plasmas* (MIT Press, Cambridge, 1964).
- [54] Y. Chao, L. Zhu, and H. Yuan, Rayleigh-Taylor instability of viscous liquid films under a temperature-controlled inclined substrate, *Phys. Rev. Fluids* **6**, 064001 (2021).
- [55] D. Benney, Long waves on liquid films, *J. Math. Phys.* **45**, 150 (1966).
- [56] C. Canuto, M. Y. Hussaini, A. Quarteroni, T. A. Zhang, Jr., *Spectral Methods in Fluid Dynamics* (Springer Science & Business Media, Berlin, 2012).
- [57] K. Atkinson, *An Introduction to Numerical Analysis* (Wiley, New York, 1991).
- [58] L. B. Smolka, J. North, and B. K. Guerra, Dynamics of free surface perturbations along an annular viscous film, *Phys. Rev. E* **77**, 036301 (2008).
- [59] J. G. Oldroyd, On the formulation of rheological equations of state, *Proc. R. Soc. London, Ser. A* **200**, 523 (1950).
- [60] S. S. Datta *et al.*, Perspectives on viscoelastic flow instabilities and elastic turbulence, *Phys. Rev. Fluids* **7**, 080701 (2022).
- [61] J. B. Boreyko and C.-H. Chen, Self-propelled dropwise condensate on superhydrophobic surfaces, *Phys. Rev. Lett.* **103**, 184501 (2009).
- [62] C. Yang, Y. Yu, L. Shang, and Y. Zhao, Flexible hemline-shaped microfibers for liquid transport, *Nat. Chem. Eng.* **1**, 87 (2024).